high plant biomass (*7*, *8*, *25*). However, in the case of nitrogen addition the negative relationship between productivity and species richness has been shown to diminish over time [(*26*), but see (*27*, *28*)]. It may be that low species richness in high-productivity conditions arises in part because most such habitats are anthropogenic, and there are few species in the local pool adapted to these conditions (*11*, *12*). If so, it is possible that species will eventually immigrate from distant pools, so that the right-hand part of the hump will then flatten out.

We have shown a global-scale concave-down unimodal relationship between biomass production and richness in herbaceous grassland communities. However, the original HBM (*7*) is vaguely articulated by the standards of modern ecological theory, and it is clear that more work is needed to determine the underlying causal mechanisms that drive the unimodal pattern (*1*, *6*, *17*, *18*). We recognize that, in our study and many others, productivity accounts for a fairly low proportion of the overall variation in richness and that many other drivers of species richness exist (*28*–*30*). Accordingly, we echo the call of Adler *et al.* (*1*) for additional efforts to understand the multivariate drivers of species richness.

## REFERENCES AND NOTES


1. P. B. Adler *et al.*, *Science* **333**, 1750–1753 (2011).
2. J. D. Fridley *et al.*, *Science* **335**, 1441 (2012).
3. X. Pan, F. Liu, M. Zhang, *Science* **335**, 1441 (2012).
4. J. B. Grace *et al.*, *Science* **335**, 1441 (2012).
5. S. Pierce, *Funct. Ecol.* **28**, 253–257 (2014).
6. J. B. Grace, P. B. Adler, W. S. Harpole, E. T. Borer, E. W. Seabloom, *Funct. Ecol.* **28**, 787–798 (2014).
7. J. P. Grime, *J. Environ. Manage.* **1**, 151–167 (1973).
8. M. M. Al-Mufti, C. L. Sydes, S. B. Furness, J. P. Grime, S. R. Band, *J. Ecol.* **65**, 759–791 (1977).
9. Q. Guo, W. L. Berry, *Ecology* **79**, 2555–2559 (1998).
10. J. H. Connell, *Science* **199**, 1302–1310 (1978).
11. M. Zobel, M. Pärtel, *Glob. Ecol. Biogeogr.* **17**, 679–684 (2008).
12. D. R. Taylor, L. W. Aarssen, C. Loehle, *Oikos* **58**, 239–250 (1990).
13. J. Oksanen, *J. Ecol.* **84**, 293–295 (1996).
14. G. G. Mittelbach *et al.*, *Ecology* **82**, 2381–2396 (2001).
15. L. N. Gillman, S. D. Wright, *Ecology* **87**, 1234–1243 (2006).
16. M. Pärtel, L. Laanisto, M. Zobel, *Ecology* **88**, 1091–1097 (2007).
17. R. J. Whittaker, *Ecology* **91**, 2522–2533 (2010).
18. L. H. Fraser, A. Jentsch, M. Sternberg, *J. Veg. Sci.* **25**, 1160–1166 (2014).
19. B. J. Cardinale, H. Hillebrand, W. S. Harpole, K. Gross, R. Ptacnik, *Ecol. Lett.* **12**, 475–487 (2009).
20. L. H. Fraser *et al.*, *Front. Ecol. Environ* **11**, 147–155 (2013).
21. Materials and methods are available as supplementary materials on *Science* Online.
22. A. K. Knapp, T. R. Seastedt, *Bioscience* **36**, 662–668 (1986).
23. B. L. Foster, K. L. Gross, *Ecology* **79**, 2593–2602 (1998).
24. M. Oesterheld, S. J. McNaughton, in *Methods in Ecosystem Science*, O. E. Sala, R. B. Jackson, H. A. Mooney, R. Howarth, Eds. (Springer-Verlag, New York, 2000), chap. 2, pp. 151–157.
25. T. K. Rajaniemi, *J. Ecol.* **90**, 316–324 (2002).
26. F. Isbell *et al.*, *Proc. Natl. Acad. Sci. U.S.A.* **110**, 11911–11916 (2013).
27. K. N. Suding *et al.*, *Proc. Natl. Acad. Sci. U.S.A.* **102**, 4387–4392 (2005).
28. T. L. Dickson, K. L. Gross, *Oecologia* **173**, 1513–1520 (2013).
29. P. Chesson, *Annu. Rev. Ecol. Syst.* **31**, 343–366 (2000).
30. K. J. Gaston, *Nature* **405**, 220–227 (2000).


## ACKNOWLEDGMENTS


We are grateful to all of the people who helped in the collection and processing of the samples, including L. Alabiso-Cahill, D. Ariunzaya, M. R. Ávila, J. C. R. Azambuja, L. Bachinger, I. Badamnyambuu, K. Baethke, J. Batbaatar, S. Ballelli, K. Bayarkhuu, G. Bertone, V. Besnyői, C. L. Bonilha, G. Boorman, R. A. X. Borges, T. Broadbent, R. Canullo, J. Carding, B. Casper, K. Castillioni, M. Cervellini, G. Charles, G. Chiara, E. Cleland, R. Cornfoot, G. Crowder, A. I. Csathó, L. Demeter, M. Demski, M. Deutschlander, S. Donnelly, A. L. P. Dresseno, S. Enkhjin, O. Enkhmandal, T. Erdenebold, L. Erdenechimeg, B. Erdenetsetseg, J. K. Fedrigo, A. C. Ferreira, Z. Foldvari, L. Fourie, B. Fraser, J. Galdi-Rosa, E. Gorgone-Barbosa, R. Greuel, A. Guido, É. György, D. Hall, A. Hassan, J. Házi, R. Henkin, S. Hoffmann, T. Jairus, M. Jankju, Ü. Jõgar, T. Jongbloets, M. Juhász, C. F. Jurinitz, V. R. Kakroudi, A. Kelemen, T. Khandarmaa, E. Khash-Erdene, C. Koch, C. Komoly, S. Kurukura, P. Liancourt, S. Lima, A. Lkhagva, M. Lucrecia Lipoma, D. Lkhagvasuren, J. Lombardi, M. Eugenia Marcotti, J. McPhee, B. McWhirter, L. Menezes, J. McCulloch, M. Mesdaghi, I. Máthé, M. Messini, M. Mistral, C. Moffat, M. Mohamed, L. Mugwedi, J. Padgham, P. Padilha, S. Paetz, S. Pagmadulam, G. Pec, C. Peconi, G. Péter, S. Piros, V. C. Pistóia, L. Pyle, M. Randall, M. Ninno Rissi, R. G. Rolim, M. Ross, T. Salarian, S. Sandagdorj, S. Sangasuren, C. Santinelli, C. Scherer, G. H. M. Silva, M. G. Silva, T. Smith, S. Solongo, F. Spada, R. Stahlmann, J. Steel, M. Sulyok, A. Sywenky, G. Szabó, L. Szabules, V. Tomlinson, J. Tremblay-Gravel, G. Ungvari, O. Urangoo, M. Uuganbayar, M. S. Viera, C. E. Vogel, D. Wallach, R. Wellstein, J. I. Withworth Hulse, and Z. Zimmermann. This work was supported in part by the Canada Research Chair Program, Canadian Foundation for Innovation (CFI), and a Natural Sciences and Engineering Research Council Discovery Grant (NSERC-DG) of Canada awarded to L.H.F., and Thompson Rivers University; a CFI and NSERC-DG awarded to J.P.; the University of Tartu, Estonia, and a European Regional Development Fund: Centre of Excellence FIBIR awarded to M.Z. and M.M.; a Hungarian National Science Foundation (OTKA K 105608) awarded to S.B.; Taylor Family-Asia Foundation Endowed Chair in Ecology and Conservation Biology and University of Mongolia's Support for High Impact Research program awarded to B.B.; the Rangeland Research Institute, University of Alberta, Canada; CONICET, Universidad Nacional de Córdoba, FONCyT, and the Inter-American Institute for Global Change Research (with support of NSF) awarded to S.D., L.E., and M.C.; a NSERC-DG awarded to J.C.; State Nature Reserve "Montagna di Torricchio" and University of Camerino, Italy; Hungarian University of Transylvania, Romania; a Fundação Grupo Boticário, Brazil (0153_2011_PR) awarded to A.F.; NSF DEB-1021158 and DEB-0950100 awarded to B.F.; UHURU: NSERC and CFI awarded to J.R.G. and the University of Wyoming; an NSERC-DG awarded to H.A.L.H.; an NSERC-DG awarded to J.K.; a National Natural Science Foundation of China grant (No. 41171417) awarded to R.L.; Conselho Nacional de Desenvolvimento Científico e Tecnológico (CNPq), Brazil (n. 307719/2012-0) awarded to S.M.; CNPq, Brazil (grants 403750/2012-1 and 307689/2014-0) awarded to V.P.; University of Florida and a NSF DEB 1149980 awarded to T.P.; Princeton Environmental Institute and a NSF DEB 1355122 awarded to R.M.P.; a CONYCIT Becas-Chile Scholarship awarded to G.C.S. Data and R scripts associated with this paper are deposited in the Dryad repository (http://datadryad.org/).


## SUPPLEMENTARY MATERIALS

www.sciencemag.org/content/349/6245/302/suppl/DC1
Materials and Methods
Supplementary Text
Figs. S1 to S6
Tables S1 and S2
References (*31*–*36*)


29 April 2015; accepted 15 June 2015
10.1126/science.aab3916


ICE SHEETS

# Reverse glacier motion during iceberg calving and the cause of glacial earthquakes


**T. Murray,[1]* M. Nettles,[2] N. Selmes,[1] L. M. Cathles,[3] J. C. Burton,[4] T. D. James,[1] S. Edwards,[5] I. Martin,[5] T. O'Farrell,[6] R. Aspey,[6] I. Rutt,[1] T. Baugé[7]**



**Nearly half of Greenland's mass loss occurs through iceberg calving, but the physical mechanisms operating during calving are poorly known and in situ observations are sparse. We show that calving at Greenland's Helheim Glacier causes a minutes-long reversal of the glacier's horizontal flow and a downward deflection of its terminus. The reverse motion results from the horizontal force caused by iceberg capsize and acceleration away from the glacier front. The downward motion results from a hydrodynamic pressure drop behind the capsizing berg, which also causes an upward force on the solid Earth. These forces are the source of glacial earthquakes, globally detectable seismic events whose proper interpretation will allow remote sensing of calving processes occurring at increasing numbers of outlet glaciers in Greenland and Antarctica.**


One-third to one-half of Greenland's total mass loss occurs through iceberg calving at the margins of tidewater-terminating glaciers (*1*, *2*). Recent rapid changes in glacier dynamics are associated with increased calving rates (*3*–*5*) and increased rates of glacial earthquakes (*6*). At large glaciers with near-grounded termini, calving typically occurs when buoyancy forces cause icebergs that are the full thickness of the glacier to capsize against the calving front (*6*–*9*). This type of calving is associated with glacial earthquakes (*6*, *7*, *10*), long-period seismic emissions of magnitude ~5 that are observed globally (*11*). These earthquakes have expanded northward and increased sevenfold in number during the past two decades (*6*, *12*, *13*), tracking changes in glacier dynamics, the retreat of glacier fronts, and increased mass loss (*6*, *14*). Buoyancy-driven calving represents an increasingly important source of dynamic mass loss (*6*–*8*) as glacier fronts throughout Greenland have retreated to positions near their grounding lines (*15*). However, because of the difficulty of instrumenting the immediate near-terminus region of these highly active glaciers, few direct observations of the calving process are available, limiting development of the deterministic calving models required for improved understanding of controls on dynamic ice-mass loss. Detailed knowledge of the glacial earthquake source would allow quantification of calving processes for a large

class of Greenland glaciers, as well as for glaciers in several regions of Antarctica (*13*).

Agreement on the source mechanism of glacial earthquakes is limited. Analysis of long-period seismic data shows that a sub-horizontal force acts approximately perpendicular to the glacier calving front during the earthquakes (*6*, *13*). The observed seismic signal is generated over a period of 1 min or more (*6*, *11*, *16*), much longer than the source duration for tectonic earthquakes of similar size (*17*). Some authors favor a model in which momentum transfer produces a force acting in the upglacier and then downglacier directions as a newly calved iceberg overturns, accelerates away from the calving front, and subsequently decelerates (*6*, *10*, *13*, *18*). Others suggest that the seismic signal arises from the iceberg scraping along the calving front or fjord bottom (*7*) or colliding with the glacier terminus (*19*). Hydrodynamic interactions with fjord water may be important (*20*) but are little explored. Analytical investigations admit more than one possible mechanism for the earthquakes (*18*), and no persuasive explanation has been presented for the vertical component of the earthquake force. We combined geodetic, seismic, and laboratory data to identify the forces acting during calving at large glaciers and to document the source of the associated seismic signals.

We recorded geodetic data at the calving margin of Helheim Glacier (Fig. 1) (*9*), a major outlet of the Greenland Ice Sheet, during 55 days in July–September 2013. A wireless network of on-ice Global Positioning System (GPS) sensors (*21*) captured glacier motion with centimeter-level accuracy at a high temporal sampling rate in positions very close to the calving front (*22*). Hourly images from two cameras located ~4 km down-fjord from and looking at the calving front were used in stereo configuration to obtain the three-dimensional geometry of the calving front and calved icebergs (*8*, *22*). Data from the global seismographic network were analyzed for the same time period to identify glacial earthquakes (*13*, *23*) and obtain source parameters (*11*), including the orientation of the force active during the earthquake and the amplitude and centroid time, $t_c$, of a centroid-single-force (CSF) history of prescribed shape (*22*).

The glacier retreated ~1.5 km in a series of calving events during the observing period. We identified 10 large calving events from the camera images. All coincided with glacial earthquakes; in two cases, two earthquakes occurred between subsequent images. During the earthquakes, the region near the calving front showed a dramatic reversal of flow, moving upglacier for several minutes while simultaneously moving downward (Fig. 2 and fig. S1). The horizontal and vertical motion then rebounded rapidly.

Observations from a glacial earthquake occurring on day of year (DOY) 206 at 03:13:47 UTC are shown in Fig. 2, A and C. Analysis of camera images indicates ice loss of 0.461 ± 0.009 $km^2$ (Fig. 1) at a location of ice thickness 0.79 km, yielding an iceberg volume of 0.36 $km^3$ with an aspect ratio of 0.23. The earthquake had a CSF amplitude of $0.24 \times 10^{14}$ kg-m, with the force oriented 64°W (Fig. 1) and 9° above horizontal. GPS sensor 1 (Fig. 1) showed a pre-earthquake flow speed of 29 m/day. Immediately before the earthquake centroid time, the sensor reversed its direction and moved upglacier at ~40 m/day (displacement = 9 cm) and downward (displacement = 10 cm). The reversed motion was sustained for ~200 s and was followed by a downglacier rebound at ~190 m/day (displacement = 20 cm) and upward movement (displacement = 16 cm) for ~90 s. Similar temporally coincident signals were detected by nearby sensors 6 and 15 (Fig. 1 and fig. S1).

Glacier deflection for a calving event on DOY 212 (Fig. 1) is shown in Fig. 2, B and D. We observed similar responses for all glacial earthquake–iceberg calving events during which GPS sensors recording data of adequate quality were located within 500 m of the calved block (a total of nine glacial earthquakes and eight image pairs). These events occurred on DOY 205, 206 (three events), 207, 211, 212, and 226 and were detected by multiple GPS sensors (further examples in fig. S1).

The earthquake centroid times occurred at or near the end of the glacier's rapid rebound phase, such that the upglacier earthquake force aligned in time with the reverse motion of the glacier. The horizontal glacier deflection is consistent with a model in which the reaction force on the glacier caused by seaward acceleration of the newly calved iceberg compresses the glacier front elastically. The front then rebounds as the force decreases and reverses polarity during iceberg deceleration. The glacier front thus acts as a spring, compressing and re-extending in phase with the applied force, which is the horizontal component of the seismic source.

The downward deflection of the glacier front occurred in a region where vertical motion of the GPS sensors at tidal frequencies showed that the glacier is ungrounded and seawater is present beneath it. Iceberg rotation is likely to cause a low-pressure zone in the opening cavity between the iceberg and the glacier front. This pressure decrease would lower the load on the bedrock, resulting in an upward force acting on the solid Earth, as observed in our seismic analysis. A pressure decrease near the calving front would apply a net downward force on the glacier terminus, lowering the glacier surface in a manner similar to that occurring twice each day when the ocean tides draw down the water level. At sensors experiencing earthquake deflections, we observed tidal variations in the glacier's vertical position of ~0.1 m per 1 m of tidal amplitude. The calving-related deflection of the glacier surface was ~0.1 to 0.16 m, suggesting a change in water pressure equivalent to a water-height change of ~1 to 1.6 m, or roughly 1 to $2 \times 10^4$ Pa.

No observations of pressure or water-level variations are available from the region in the fjord immediately in front of the glacier, where thick ice mélange (Fig. 1) prohibits instrumentation. However, results from analog laboratory experiments allowed us to evaluate our inferences (*22*). A model glacier "terminus" was secured at one end of a water-filled tank, and plastic "icebergs" made from low-density polyethylene were placed flush against the terminus and allowed to capsize spontaneously under the influence of gravitational and buoyancy forces (*24*) (Fig. 3). Sensors embedded in the model glacier terminus monitored pressure in the water column and the force exerted on the terminus during iceberg capsize.

The measured force on the terminus as the icebergs began to capsize was oriented in the upglacier direction and slowly increased as the icebergs rotated. As the icebergs neared horizontal, the force decreased rapidly. Pressure at the terminus decreased as the icebergs rotated, increasing again as the icebergs neared horizontal. Once the icebergs lost contact with the terminus, the measured force and pressure began to oscillate as a result of induced wave action in the tank.

We scaled up the measured forces and pressures to match the dimensions of icebergs calved at Helheim Glacier (Fig. 3). The laboratory data scale by powers of the ratio of the iceberg height in the field to the iceberg height in the laboratory (*20*, *24*). The scaled peak force agreed well with typical values inferred from earthquake analysis (~$10^{11}$ N). The scaled peak pressure drop (~$5 \times 10^4$ Pa) applied over an area corresponding to the iceberg's map-view dimensions yielded an upward-directed force consistent with the seismically inferred vertical force component, such that the total force acting on the solid Earth was oriented ~10° above horizontal. Computation and inversion of synthetic seismograms from the scaled force and pressure data confirmed the consistency of the laboratory model with real-world data.

We used the scaled force and pressure to predict the deformation of the terminus region (*22*). The total force ($F_{tot}$) per unit area ($A_F$) acting on the calving region produces a horizontal, linear deflection orthogonal to the calving front, such that $F_{tot}/A_F = E\Delta L/L$, where $E$ is the Young's modulus of glacial ice. The value of $L$ is chosen to provide the best match to the glacier position data. This length-scale probably represents the distance from the terminus to the grounding zone. We modeled the ungrounded section of the glacier as an elastic beam of length $L$ loaded by the vertical force created by the pressure drop. The inferred distances $L$ are a few kilometers, consistent with values estimated from GPS data.

Glacier displacements predicted from the scaled laboratory data for iceberg dimensions corresponding to a calving event on DOY 206 (Fig. 1 and Fig. 2A) are shown in Fig. 3. Agreement with the observed glacier displacement was very good, particularly during the time over which the force acted in the upglacier direction (until the earthquake centroid time). After this time, the

[1]Glaciology Group, Department of Geography, College of Science, Swansea University, Swansea SA2 8PP, UK. [2]Lamont-Doherty Earth Observatory, Columbia University, New York, NY 10964, USA. [3]Department of Atmospheric, Oceanic and Space Sciences, University of Michigan, Ann Arbor, MI 48109, USA. [4]Department of Physics, Emory University, Atlanta, GA 30322, USA. [5]School of Civil Engineering and Geosciences, Newcastle University, Newcastle upon Tyne NE1 7RU, UK. [6]Department of Electronic and Electrical Engineering, University of Sheffield, Sheffield S1 3JD, UK. [7]Thales UK, Research and Technology, Worton Drive, Reading, Berkshire RG2 0SB, UK.
***Corresponding author. E-mail: t.murray@swansea.ac.uk**

laboratory-derived prediction was dominated by oscillations of the water column in the tank, which did not contain the thick layer of ice mélange present in Helheim Fjord that would be expected to dampen such high-frequency oscillations.

We conclude that as large icebergs rotate and accelerate away from the glacier calving front (Fig. 4), the reaction force—which is the horizontal component of the earthquake force—compresses the glacier front elastically, overcoming normal downglacier flow and temporarily reversing the motion of the glacier. Hydrodynamic interaction of the iceberg with the fjord water rapidly reduces pressure behind the rotating iceberg, resulting in an upward force on the solid Earth that is the

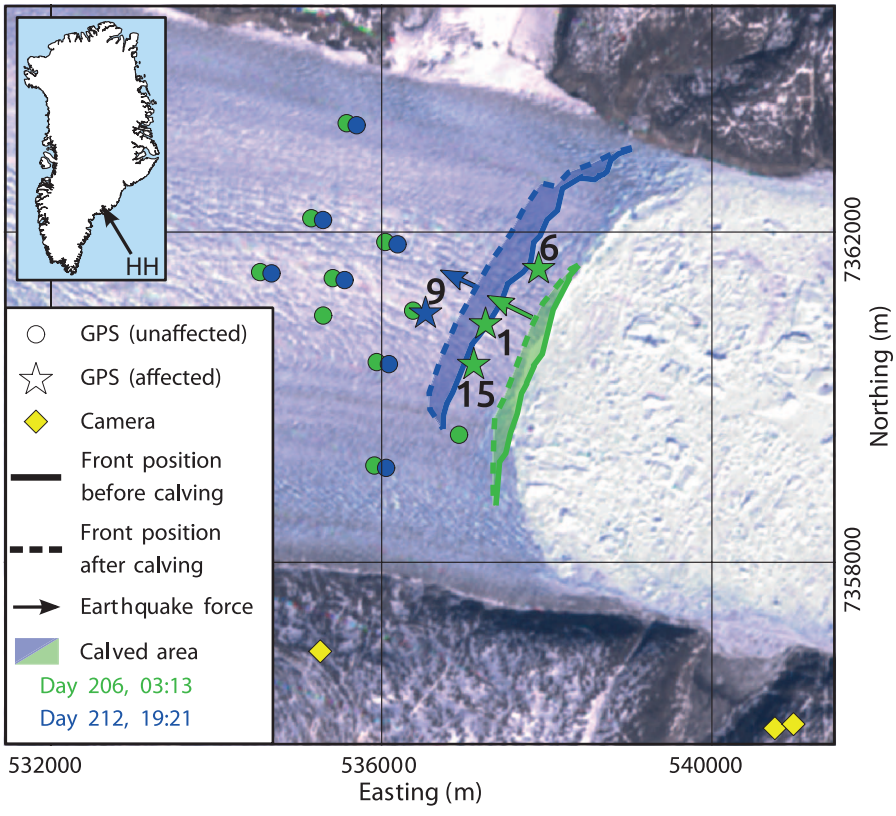


**Fig. 1. Helheim Glacier, position of sensors, and seismic force directions.** The location of GPS sensors and icebergs calved at Helheim Glacier (HH) for glacial earthquake events at 03:13 UTC on DOY 206 2013 and 19:21 UTC on DOY 212 2013 are superimposed on a Landsat 7 image from DOY 167 2013. "Affected" sensors exhibit earthquake-related deflections. Scan-line-corrector failure stripes have been removed for clarity. Glacier flow is from left to right; bright white mélange (a mix of iceberg fragments and sea ice) can be seen in front of the calving margin. Calving-front positions were obtained from photogrammetric digital elevation models derived from cameras. Positions are meters in Universal Transverse Mercator zone 24N.

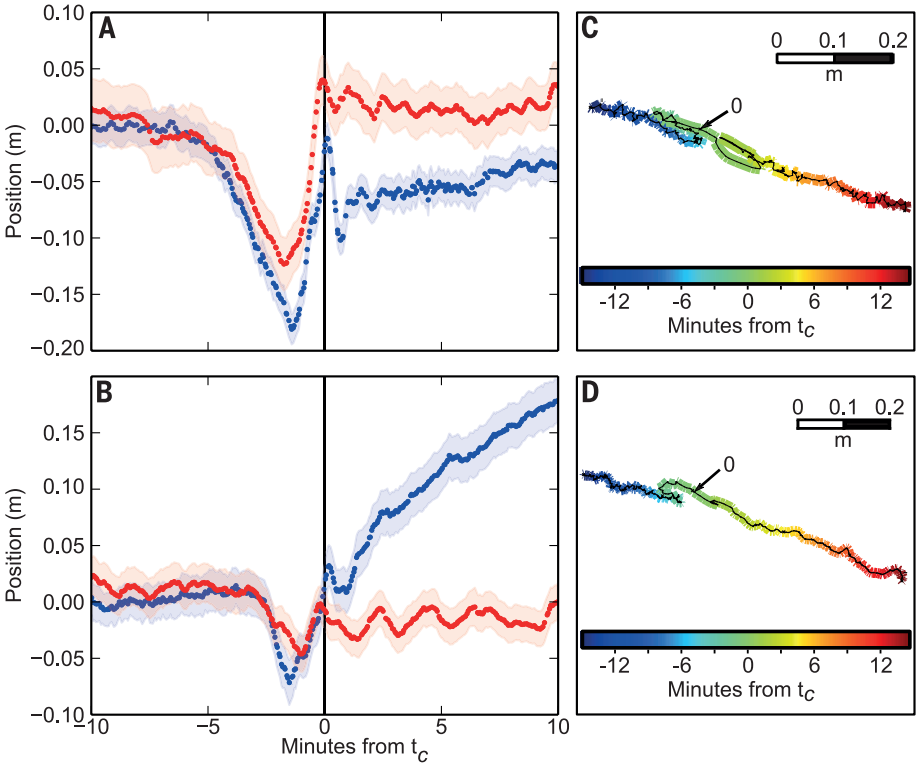


**Fig. 2. Response of GPS sensors on glacier at the time of glacial earthquakes.** (**A**) Sensor 1 at 03:13 UTC on DOY 206 2013. (**B**) Sensor 9 at 19:21 UTC on DOY 212 2013. Blue dots show detrended along-flow displacement; red dots show height. Shading shows 1σ position errors. Horizontal displacement has trends from 30 to 10 min before $t_c$ removed (A = 28.9 m/day, B = 24.6 m/day). Height has mean removed. (**C** and **D**) Plan view of GPS traces shown in (A) and (B) during the 30 min surrounding $t_c$ (marked as 0).

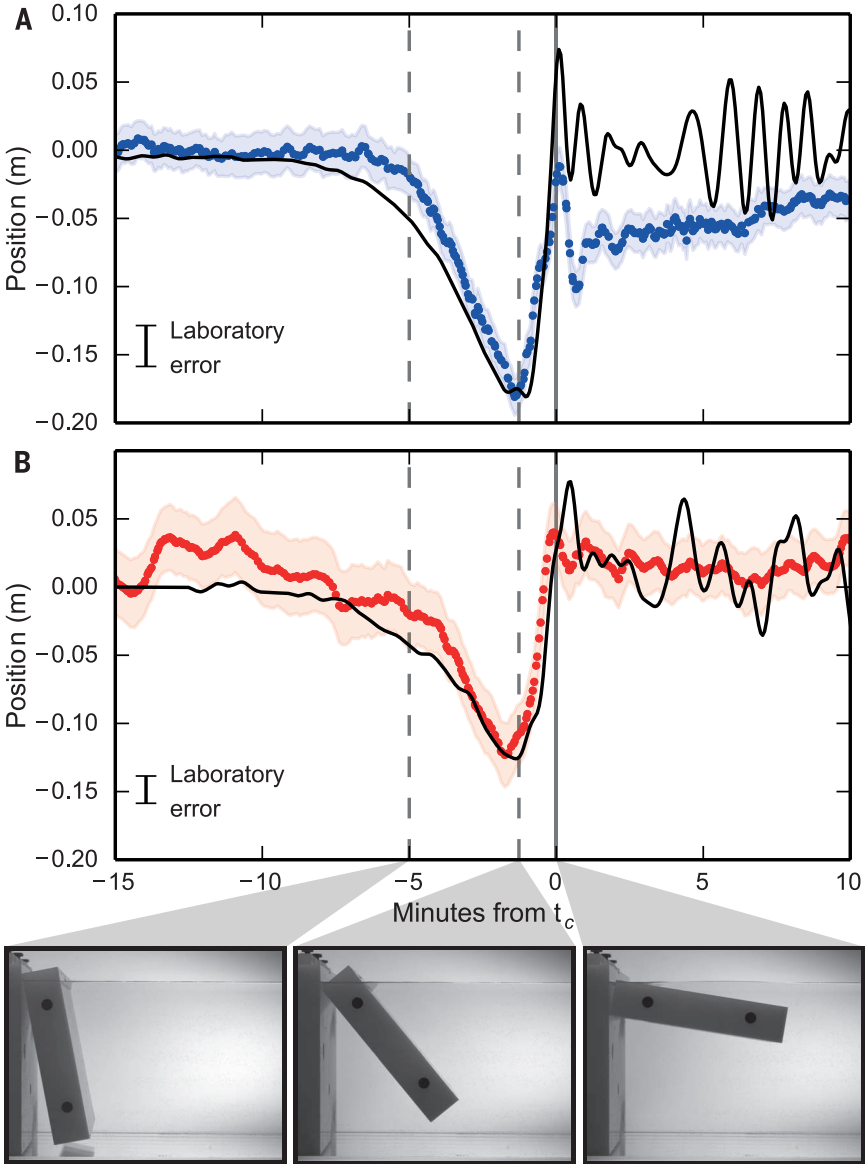


**Fig. 3. Scaled laboratory data from glacier "terminus" during "iceberg" capsize event, compared with field observations.** (**A**) Horizontal displacement scaled from force (black line) compared with downflow GPS data (blue). (**B**) Vertical displacement scaled from pressure (black line) compared with vertical GPS data (red). Errors in laboratory data are standard deviation calculated from repeated capsize events. GPS data shown are as in Fig. 2A. Photographs show stages of capsize at times marked by dashed lines and (solid gray line) $t_c$. The aspect ratio of the model iceberg is 0.22.

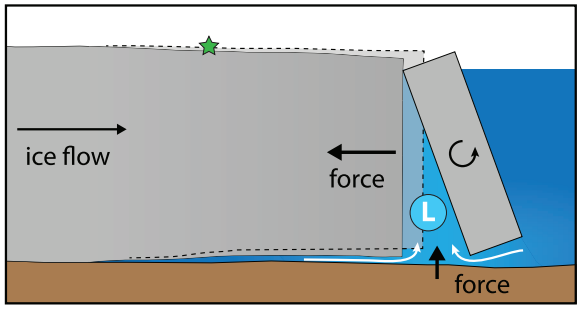


**Fig. 4. Cartoon of glacier terminus during calving event.** Glacier deflection caused by a capsizing iceberg is shown relative to the initial glacier position (dotted line). Acceleration of the iceberg to the right exerts a force in the upglacier direction (left), leading to reverse motion of the GPS sensors (green star). Reduced pressure behind the iceberg (L) draws water from beneath the glacier and from the proglacial fjord, pulling the floating portion of the glacier downward and exerting an upward force on the solid Earth.

vertical force observed in the earthquake. The lowered water pressure draws down the ungrounded glacier margin, pulling the glacier surface downward during the earthquake.

Our results document the forces active during an increasingly important class of calving events and definitively identify the processes that cause glacial earthquakes. This understanding of glacier calving and glacial earthquakes opens the potential for remote quantitative characterization of iceberg calving and calving rates, as well as improved models for ice-ocean interaction.

## REFERENCES AND NOTES


1. M. van den Broeke *et al.*, *Science* **326**, 984–986 (2009).
2. E. M. Enderlin *et al.*, *Geophys. Res. Lett.* **41**, 866–872 (2014).
3. I. Joughin, W. Abdalati, M. Fahnestock, *Nature* **432**, 608–610 (2004).
4. A. Luckman, T. Murray, R. de Lange, E. Hanna, *Geophys. Res. Lett.* **33**, L03503 (2006).
5. I. M. Howat, I. Joughin, T. A. Scambos, *Science* **315**, 1559–1561 (2007).
6. S. A. Veitch, M. Nettles, *J. Geophys. Res.* **117**, F04007 (2012).
7. J. M. Amundson *et al.*, *Geophys. Res. Lett.* **35**, L22501 (2008).
8. T. D. James, T. Murray, N. Selmes, K. Scharrer, M. E. O'Leary, *Nat. Geosci.* **7**, 593–596 (2014).
9. T. Murray *et al.*, *J. Geophys. Res. Earth Surf.* 10.1002/2015JF003531 (2015).
10. M. Nettles *et al.*, *Geophys. Res. Lett.* **35**, L24503 (2008).
11. G. Ekström, M. Nettles, G. A. Abers, *Science* **302**, 622–624 (2003).
12. G. Ekström, M. Nettles, V. C. Tsai, *Science* **311**, 1756–1758 (2006).
13. M. Nettles, G. Ekström, *Annu. Rev. Earth Planet. Sci.* **38**, 467–491 (2010).
14. I. Joughin *et al.*, *J. Geophys. Res.* **113**, F01004 (2008).
15. I. M. Howat, A. Eddy, *J. Glaciol.* **57**, 389–396 (2011).
16. V. C. Tsai, G. Ekström, *J. Geophys. Res.* **112**, F03S22 (2007).
17. G. Ekström, E. R. Engdahl, *J. Geophys. Res.* **94**, 15,499–15,519 (1989).
18. V. C. Tsai, J. R. Rice, M. Fahnestock, *J. Geophys. Res.* **113**, F03014 (2008).
19. F. Walter *et al.*, *J. Geophys. Res.* **117**, F01036 (2012).
20. J. M. Amundson, J. C. Burton, S. Correa-Legisos, *Ann. Glaciol.* **53**, 106–112 (2012).
21. I. Martin *et al.*, *IEEE Sens. J.* **14**, 3926–3931 (2014).
22. Materials and methods are available as supplementary materials on *Science* Online.
23. G. Ekström, *Bull. Seismol. Soc. Am.* **96**, 1201–1212 (2006).
24. J. C. Burton *et al.*, *J. Geophys. Res.* **117**, F01007 (2012).


## ACKNOWLEDGMENTS

This work was supported by the Natural Environment Research Council UK grant NE/I007148/1. T.M. is currently supported by a Royal Society Leverhulme Trust Senior Research Fellowship. T.D.J. was supported by the Climate Change Consortium of Wales (C3W). M.N. was supported by U.S. NSF grant EAR-1249167. L.M.C. is currently supported by the Michigan Society of Fellows. J.B. and L.M.C. were supported and the laboratory equipment was developed with support from NSF grant ANT-0944193. A. Everett is thanked for assistance in the field and L. Kaluzienski for assistance with laboratory data. We thank the staff of the Civil Engineering and Geosciences workshop, Newcastle University, for GPS sensor construction. We acknowledge the use of bed data from the Center for Remote Sensing of Ice Sheets, generated with support from NSF grant ANT-0424589 and NASA grant NNX10AT68G, and the use of seismic data from the Incorporated Research Institutions for Seismology (IRIS)–U.S. Geological Survey Global Seismographic Network, Geoscope, Geofon, Mednet, and the Greenland Ice Sheet Monitoring Network. A 2013 lidar survey flown by the Natural Environment Resource Council Airborne Remote Sensing Facility was used in the processing of photographs. Seismic waveforms are available from the IRIS Data Management Center (NSF EAR-1261681); GPS data are available from UNAVCO (NSF EAR-1261833).

## SUPPLEMENTARY MATERIALS

www.sciencemag.org/content/349/6245/305/suppl/DC1
Materials and Methods
Fig. S1
References (*25*–*41*)
Data Table S1

10 March 2015; accepted 12 June 2015
Published online 25 June 2015
10.1126/science.aab0460